







Article

Similarities and differences among selected gemmological varieties of chalcedony: chemistry, mineralogy and microstructure

Sara Monico¹ , Marco Cantaluppi¹ , Valeria Diella² , G. Diego Gatta¹ , Ilaria Adamo³, Patrizia Fumagalli¹ and Nicoletta Marinoni¹

¹Department of Earth Sciences “Ardito Desio”, University of Milan, Via Botticelli 23, 20133 Milan, Italy; ²National Research Council, Institute of Environmental Geology and Geoengineering (IGAG), Section of Milan, via Botticelli 23, 20133 Milan, Italy; and ³Istituto Gemmologico Italiano (IGI), Piazza San Sepolcro 1, 20123 Milan, Italy

Abstract

This study describes a new variety of chalcedony with a unique inhomogeneous bluish green hue, named aquaprase. It was discovered in Africa and is considered to be a valuable addition to the gem trade. A multi-methodological approach was used to examine its chemistry, mineralogy and microstructure, which were then compared to those of chrysoprase and agate, two of the most popular varieties of chalcedony. Optical microscopy revealed a complex microstructural heterogeneity in the different colour intensity areas/bands of aquaprase and agate, whereas chrysoprase exhibited a more homogeneous coexistence of micro- and cryptocrystalline quartz. High-resolution synchrotron XRD was essential for highlighting the complex assemblage of various types of α -quartz in aquaprase and agate (which differ in terms of crystal size and/or cell parameters). Micro-Raman spectroscopy revealed α -quartz and moganite in all three varieties of chalcedony and the presence of the nickel-bearing layered silicate mineral, willemseite, in chrysoprase, which is responsible for its green colouration. The chemical analysis displayed a homogeneous composition of agate, as well as high levels of nickel content in the chrysoprase variety. Aquaprase showed significant amounts (ppm by weight) of trace elements (Al, Mg, Na, K, Ca, Ti, U and Fe) characteristic of its formation environment, as well as high values of Cr, which are thought to be the cause of its bluish green colouration.

Keywords: gemstones; chalcedony; aquaprase; chrysoprase; agate; composition; microstructures

(Received 18 April 2023; accepted 28 November 2023; Associate Editor: Juraj Majzlan)

Introduction

Microcrystalline quartz occurs ubiquitously in geological environments and is generally classified by compositional and structural features (Graetsch, 1994). Microcrystalline fibrous varieties are called chalcedony and consist of 50–100 nm α -quartz crystallites (Miehe *et al.*, 1984; Cady *et al.*, 1998; Ríos *et al.*, 2001) arranged in a fibre-like texture. Traditionally, chalcedony has been subdivided into two groups (Michel-Lévy and Munier-Chalmas, 1892): (1) length-fast chalcedony, showing fibres and with crystallites having their *c*-axis orientated perpendicularly to the fibre axis (the fibrous ‘chalcedony crystals’ have polysynthetic twinning according to the Brazil-twin law, with the *c*-axis of quartz fibres twisted about the fibre axis) (Miehe *et al.*, 1984; Heaney, 1993) and (2) length-slow chalcedony (or quartzine), with fibres composed of crystallites that have their *c*-axis orientated parallel to the fibre axis (Schmidt *et al.*, 2013b).

In contrast to macrocrystalline quartz, chalcedony often contains H₂O in the range of 1 to 2 wt.%, both as molecular H₂O and as silanol groups (Flörke *et al.*, 1982). Together with

chalcedony, it is common to find a polymorph of silica, called moganite, which exhibits a monoclinic crystal lattice formed by a structure of left and right quartz lamellae, alternating at the unit cell scale (Flörke *et al.*, 1976; Miehe *et al.*, 1984, Miehe, 1986; Miehe and Graetsch, 1992). The structure has therefore been associated with Brazil-law twin boundaries, as they are found frequently in the quartz crystallites of chalcedony (Miehe *et al.*, 1984; Cady *et al.*, 1998). Moganite is present in chalcedony at 5 to 20 wt.% (Heaney and Post, 1992; Gliozzo, 2019).

The most favourable geological settings for the formation of chalcedony are low temperatures and under near-surface conditions (White and Corwin, 1961; Cady *et al.*, 1998). Chalcedony is found typically in sedimentary environments, where it precipitates within rock pore spaces and fractures from percolating silica-rich solutions. Additionally, it can form through hydrothermal activity and in volcanic environments, often filling cavities as a mineral deposit.

Chalcedony has several varieties, based on colour, which have been appreciated and used for making jewellery and ornaments since ancient times. Agate is one of the most famous varieties of chalcedony because of its wide spectrum of colours (white, yellow, red, green and blue) and spectacular banded features (Graetsch, 1994; Gliozzo, 2019). It can be regarded as banded chalcedony, which is intergrown or intercalated with other silica phases. Moreover, agate often contains considerable amounts of mineral inclusions and these impurities can form spectacular

Corresponding author: Sara Monico; Email: sara.monico1@unimi.it

Cite this article: Monico S., Cantaluppi M., Diella V., Gatta G.D., Adamo I., Fumagalli P. and Marinoni N. (2024) Similarities and differences among selected gemmological varieties of chalcedony: chemistry, mineralogy and microstructure. *Mineralogical Magazine* 88, 136–146. <https://doi.org/10.1180/mgm.2023.92>

© The Author(s), 2024. Published by Cambridge University Press on behalf of The Mineralogical Society of the United Kingdom and Ireland. This is an Open Access article, distributed under the terms of the Creative Commons Attribution licence (<http://creativecommons.org/licenses/by/4.0/>), which permits unrestricted re-use, distribution and reproduction, provided the original article is properly cited.

internal structures or be responsible for the different colouration of agates. The chemical and mineralogical complexity of agate is the result of its formation conditions.

Another variety, much appreciated for its charming apple green colour, is chrysoprase (Caucia *et al.*, 2016). It has been used since ancient times (Hatipoğlu *et al.*, 2011) and its most famous localities of extraction are in Australia (Jiang *et al.*, 2021). The origin of chrysoprase colour is a controversial topic (Jiang *et al.*, 2021): some authors believe that the colour can be attributed to the presence of finely dispersed nickel-bearing layered silicate minerals from the stones that usually occur in the chrysoprase deposits, such as willemseite (Eggleton *et al.*, 2011) or 'kerolite' (Sachanbiński *et al.*, 2002) and 'pimelite' (Čermáková *et al.*, 2017; Jiang and Guo, 2021), however, the latter two have now been discredited as formal mineral names (Eggleton *et al.*, 2011). Others have claimed that the green colour is due to the presence of evenly distributed bunsenite (NiO) crystallites within the gemstone (Jiang and Guo, 2021).

In 2013, the Greek gem explorer and trader Yianni Melas discovered a new bluish green variety of chalcedony in Africa, which is commercially known as aquaprase (Renfro, 2015). AQUAPRASE™ is also a trademark used to distribute and market this bluish green chalcedony. Aquaprase has a translucent transparency, typical of chalcedony, and its natural bluish green colour is inhomogeneous, because of the presence of intense and colourless areas with dark brown inclusions due to a combination of the mineral with the rock matrix.

In this study, we compare the chemical, mineralogical and microstructural features of this new variety of chalcedony (aquaprase) with selected samples of agate and chrysoprase.

Materials

Twenty samples of chalcedony belonging to three different varieties, i.e. aquaprase, chrysoprase and agate, were selected, consisting of both polished cabochon-cut gemstones and roughs. Representative samples are shown in Fig. 1, and details given in Table 1. Aquaprase samples have been labelled as AQ_x, chrysoprase as CR_x and agate as AG_x, respectively, and x refers to the sample number.

Experimental methods

Thin sections were studied under a Leitz polarised-light microscope, which was connected to a 51 MP camera. The software

Affinity (by Serif (Europe) Ltd, UK) was used to merge photos and create overviews of the samples.

Laboratory powder X-ray diffraction (XRD) data were collected at the Department of Earth Sciences of the University of Milan, Italy, with a Panalytical X'Pert-PROMPD X'Celerator powder X-ray diffractometer, using CuK α radiation ($\lambda = 1.5406 \text{ \AA}$), at a beam voltage of 40 kV and a current of 40 mA. Bragg-Brentano diffraction patterns were collected over the 10–60° range of the scattering angle 2θ , with steps of $0.01^\circ 2\theta$ and a counting time of 40/60 s per step.

To overcome the main drawbacks of the laboratory XRD experimental set up, such as strong peak overlapping (i.e. moganite vs quartz), peak broadening, and preferred orientation, high-resolution synchrotron powder X-ray diffraction was undertaken, thus allowing detection of minor phases together with a more reliable quantitative phase analysis. The high-resolution synchrotron XRD experiments were performed at beamline ID22 of the European Synchrotron Radiation Facility (Grenoble, France), using a Debye-Scherrer configuration with a wavelength of $\lambda = 0.35456 \text{ \AA}$, selected by a double-crystal Si (111) monochromator. Samples were loaded in borosilicate glass capillaries (diameter = 2 mm), spinning during data collection. The overall measuring time per sample was 100 min, to obtain very good statistics over the angular $1.0\text{--}37.9^\circ$ in 2θ , or over the interplanar distance range from 20 to 0.5 \AA . The data from the monochromator Multi-Analyser Si (111) Stage, coupled with the nine scintillation detectors, were normalised and summed to a 0.002° step size with local software to produce the final raw data.

The Rietveld full profile fit of the XRD patterns was performed using MAUD software (Lutterotti *et al.*, 2007; Saville *et al.*, 2021). Unit cell parameters, zero shift error, crystallite size, microstrain, individual scale factor and a background function (Chebyshev polynomial, three terms) were refined. The refinement of the above-mentioned parameters was performed till an improvement of the fitting was observed. Crystal structural models used are listed below, from the open-access Crystal Open Database (COD) (Gražulis *et al.*, 2012): quartz (I, II, III) (ref. COD: 2300370) (Lignie *et al.*, 2012); moganite (ref. COD: 9002648), (Heaney and Post, 2001); palygorskite (ref. COD: 1533365), (Chiari *et al.*, 2003); pyrophyllite (ref. COD:1011153) (Gruner, 1934); phlogopite (ref. COD: 9000111) (Steinfink, 1962); and willemseite (ref. COD: 8104532) (De Waal, 1970).

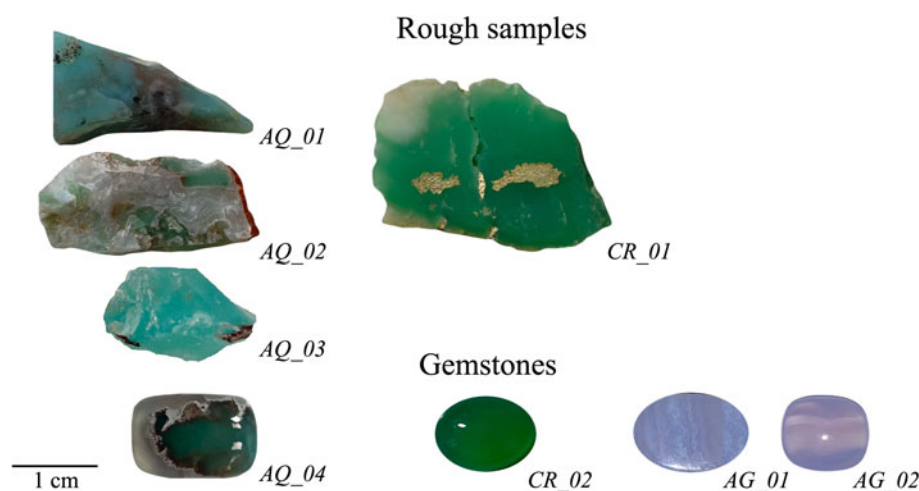


Figure 1. Eight rough and cut gemstone specimens. Aquaprase samples have been labelled as AQ_x, chrysoprase as CR_x and agate as AG_x, respectively, and x refers to the sample number.

Table 1. Chalcedony varieties, provenance and colour of the samples studied.

Sample ID	Chalcedony variety	Provenance	Colour
Rough			
AQ_01	Aquaprase	Africa	Bluish green
AQ_02	Aquaprase	Africa	Bluish green
AQ_03	Aquaprase	Africa	Bluish green
CR_01	Chrysoprase	Australia (Rockhampton region)	Green
Gemstones			
AQ_04	Aquaprase	Africa	Bluish green
CR_02	Chrysoprase	Australia (Rockhampton region)	Green
AG_01	Agate	Turkey (Yozgat region)	Light blue
AG_02	Agate	Turkey (Yozgat region)	Light blue

Micro-Raman spectroscopic analysis was carried out on thin sections, at the Department of Earth Sciences of the University of Milan, Italy, using a high-resolution confocal micro-Raman system (LabRam HR Evolution-Horiba system), attached to an Olympus petrographic microscope, with a green Nd-YAG laser source (with a wavelength of 532 nm and power of 100 mW), with very low frequency filters (ULF) and a 1 μ m spot.

Electron microprobe analyses in wavelength-dispersive mode (EMPA-WDS) were performed on thin sections, at the Department of Earth Sciences of the University of Milan, Italy, using a JEOL JXA-8200 EMP-WDS, with an accelerating voltage of 15 kV, a beam current of 5 nA, and counting times of 30 s on the peak and 10 s on the background. Concentrations of Si, Al, K, Na, Mn, Mg, Ca, Ti, Ni, Zn and Fe were measured. Raw data were corrected for matrix effects using a conventional $\Phi\rho Z$ routine in the JEOL software package (version 3.50).

The samples were analysed using laser ablation inductively coupled plasma mass spectroscopy (LA-ICP-MS) at the Laboratory of Geochemistry, Geochronology and Isotopic Geology (LASA labs) of the University of Milan. The instrument at the LASA Labs consisted of a Teledyne Analite Excite Excimer laser (air-cooled excimer laser with 193 nm ultra-short pulse) coupled to a Thermo Scientific ICP-MS iCAP RQ single quadrupole. The spot size was 65 μ m, using Nist612 glass as an external standard and ^{29}Si as an internal standard, as analysed by EMPA-WDS. Precision and accuracy estimated on the USGS basaltic glass standard BCR2 and NIST612 were better than 10%.

Chemical characterisation at the nanoscale of the samples was carried out using a FEI Tecnai F20 Field Emission Gun (FEG) microscope, working at accelerating voltage of 200 kV, available at the Transmission Electron Microscopy Laboratory of the Department of Earth Sciences “Ardito Desio” at the University of Milan. The instrumentation includes an S-Twin system lens that provides a point resolution of 0.24 nm and an energy dispersive X-ray spectrometer (EDS) with an ultra-thin window. The imaging system consists of a 626 Gatan CCD tv rate camera and a 794 Gatan slow scan camera. The detectors are embedded in the microscope control unit, and the sample holder is dual-tilt. The technical specifications of the instrumentation include: a point resolution (nm) of 0.24 and a line resolution (nm) of 0.1; an information limit (nm) of 0.15, a focal length (mm) of 1.7 and a magnification from 25 \times to 1030 \times .

Results

Optical microscopy

Significant differences in the microstructure of the three chalcedony varieties were found using optical microscopy on the thin sections (Figs 2–4).

In aquaprase, the two areas visible to the naked eye and corresponding (1) to the cloudy inhomogeneous bluish green zone and (2) to the colourless zone, exhibit different silica microstructural features in terms of grain size (from macro to crypto) and

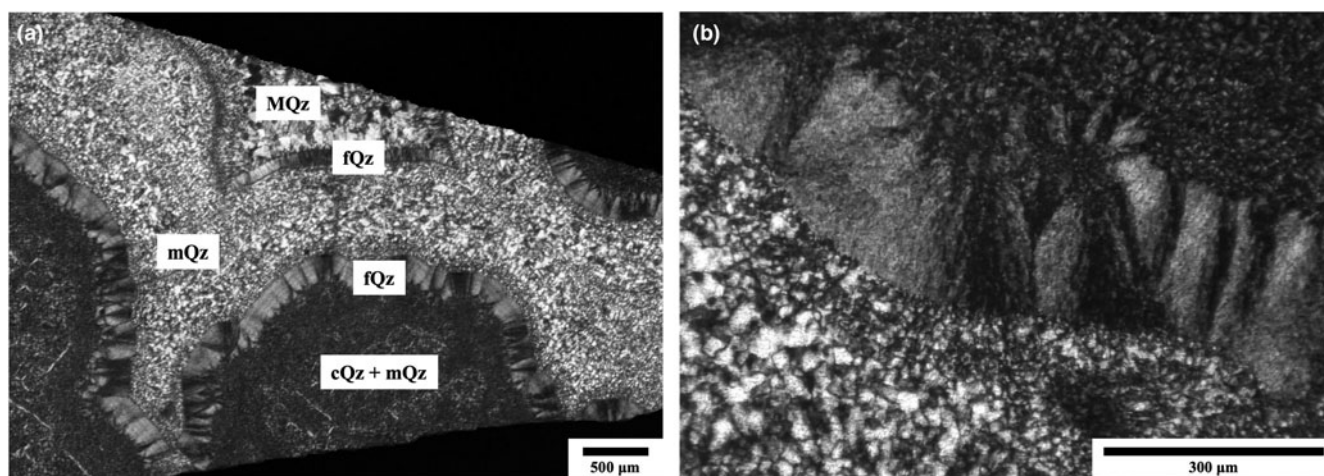


Figure 2. Optical micrographs: (a) panoramic picture of the AQ_01 aquaprase sample; and (b) details: fibrous quartz between cryptocrystalline and microcrystalline quartz (XPL, grey scale). Mineral abbreviations (Warr, 2021): MQz: macrocrystalline quartz; mQz: microcrystalline quartz; cQz: cryptocrystalline quartz; fQz: fibrous quartz; incl: inclusions.

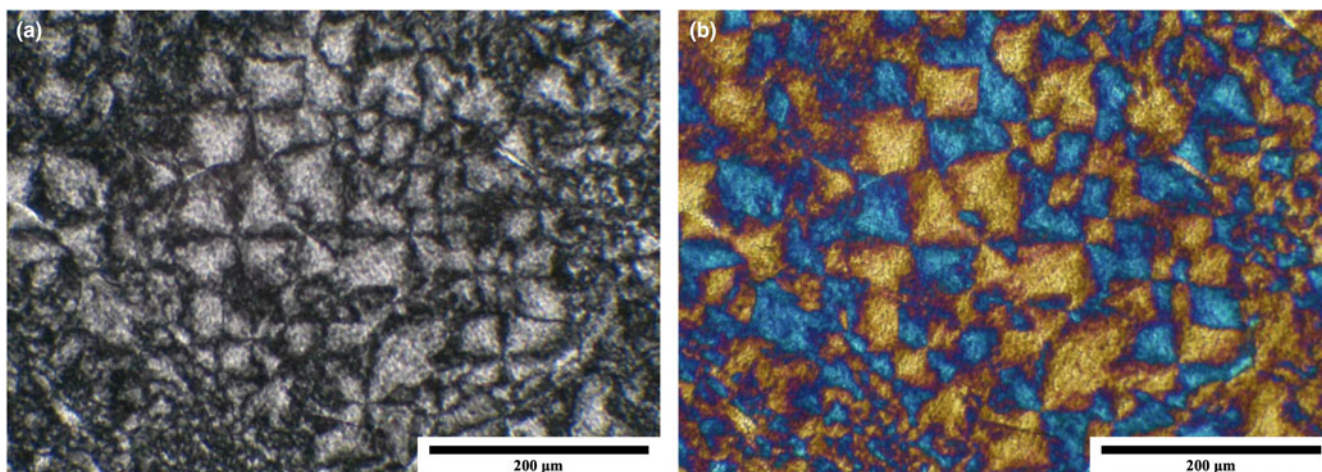


Figure 3. Optical micrographs. Details of the AQ_01 aquaprase sample: (a) length-fast spherulitic chalcedony in the cryptocrystalline quartz matrix (XPL, grey scale); (b) + gypsum plate.

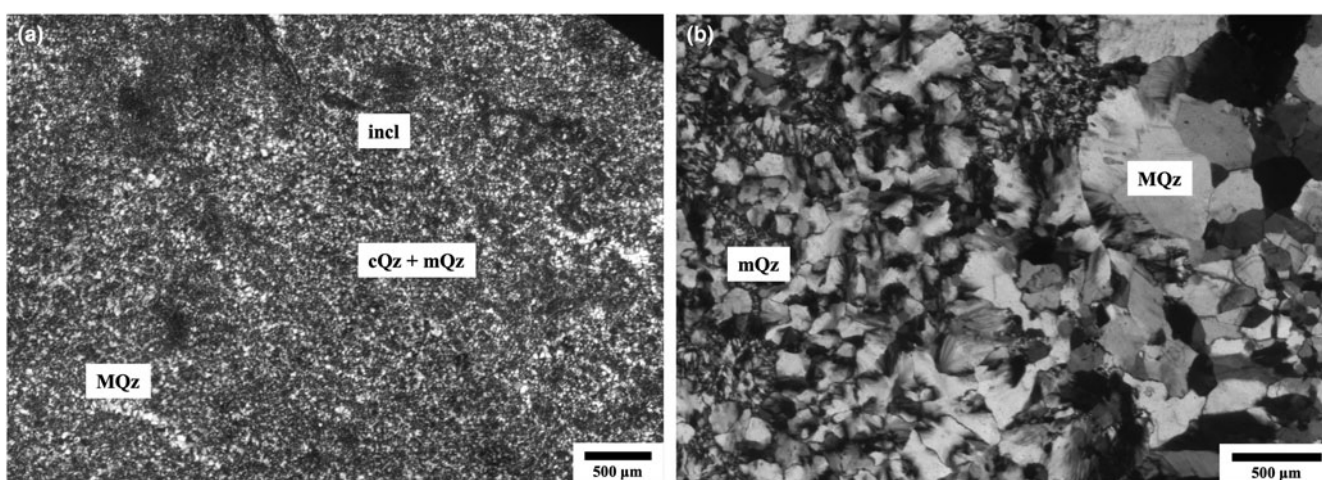


Figure 4. Optical micrographs. (a) A panoramic picture of the CR_01 chrysoprase sample and (b) a panoramic picture of the AG_01 agate sample (XPL, grey scale).

morphology (from fibrous to granular). In the former area, cryptocrystalline quartz is predominant and the nano-size of the crystals means they can not be detected individually, thus resulting in a unique mass in which linear and diagonally orientated growth of quartz and spherulites of length-fast chalcedony are observed (Figs 2, 3). Using a gypsum plate, typical interference colours of length-fast chalcedony are observed showing yellow-orange colour in fibres orientated in the NE-SW direction and blue in fibres with the NW-SE direction (crystals that are elongated parallel to their fast direction have a negative sign of elongation) (Fig. 3b). These colours would occur in the opposite directions for the length-slow chalcedony/quartzine fibres, with a positive sign of elongation. At the border between colourless and bluish green zones, bands of length-fast chalcedony in a wall-lining, with a circular shape and with smooth boundaries between nucleation centres and the cryptocrystalline mass of quartz, can be observed. Straight boundaries are evident between the adjacent growth of chalcedony (Fig. 2b). In the colourless area, microcrystalline quartz aggregates predominate with inhomogeneous grain size and different orders of magnitude in size. Length-fast chalcedony bands with a straight boundary between chalcedony quartz growths can be observed while a modest quantity of quartz

macrocrystals is found in some areas (Adams *et al.*, 1984; Gliozzo *et al.*, 2019). The transition from fibrous chalcedony to quartz crystals is smooth (Fig. 2).

The chrysoprase variety consists of crypto- to microcrystalline quartz crystals (Fig. 4a). No microstructural zoning is observed, a modest presence of macro crystals of quartz is easily observable in some areas of the micro- and cryptocrystalline aggregate. Inclusions with an opaque and dark appearance under crossed Nicols are finely dispersed within the SiO₂ matrix.

The agate variety displays bands of varying colour intensity (Fig. 4b) characterised by quartz crystals with a distinct grain size. Bands with less intense colouration are composed primarily of granular macrocrystalline quartz. Specifically, the macrocrystals have micrometre-sized lamellae, due to the episodic stages of crystal growth, typical of the so-called ‘Bambauer quartz’ (Bambauer *et al.*, 1961; Conte *et al.*, 2022) and a feathery aspect at the margins of quartz grains (Adams, 1920; Dong *et al.*, 1995). Granular quartz occurs with different orders of magnitude in size and exhibits undulose extinction (Adams *et al.*, 1984), related to the granules being polycrystalline (Adams *et al.*, 1984), denominated strained quartz (Jóźwiak-Niedźwiedzka *et al.*, 2017). This aspect is particularly evident in larger crystallites in the upper right

area of Fig. 4b. On the other hand, at the microstructural level, the bands with more intense colour are characterised by a predominance of microcrystalline and macrocrystalline quartz, significantly smaller in size than the bands with less intense colouring. In general, quartz grains also present a mosaic texture with highly irregular and interpenetrating grain boundaries (Dong *et al.*, 1995).

Powder X-ray diffraction

The laboratory powder XRD patterns of samples AQ_02, CR_01 and AG_02 are shown in Fig. 5. The results show typical chalcedony diffraction patterns characterised by α -quartz peaks and, in the case of chrysoprase and aquaprase varieties, the contribution of moganite.

The results on a different colour area of the aquaprase samples showed no differences in their mineralogical composition. On the contrary, the different Full Width at Half Maximum (FWHM) of the (101) diffraction peak of quartz suggests a slightly higher crystallinity of quartz in the colourless fraction compared to the bluish green one (Fig. 6).

The results obtained through the Rietveld Quantitative Phase Analysis (RQPA) using the MAUD software on a series of chalcedony samples are reported in Table 2. In aquaprase samples (AQ_02 and AQ_03), the high-resolution synchrotron XRD data revealed the presence of minor phases, such as palygorskite, pyrophyllite and phlogopite, and also highlights the presence of three quartz varieties, hereafter labelled as quartz I, II and III, associated with moganite (Fig. 7). Quartz I is a good fit to the main peak at $26.7^\circ 2\theta$, whereas quartz II and quartz III match the two peaks at lower and higher 2θ angles, respectively, giving rise to an asymmetry of the main diffraction peak. Quartz II and III – which are characterised by lower crystal size – represent between 58 wt.% and 68 wt.% of the crystalline phases in bluish green aquaprase samples and differ by the length of the unit cell edges: quartz II has a higher a value and a lower c value (fitting the left-most part of the peak), whereas quartz III has a lower a value and a higher c value (fitting the right-most part of the

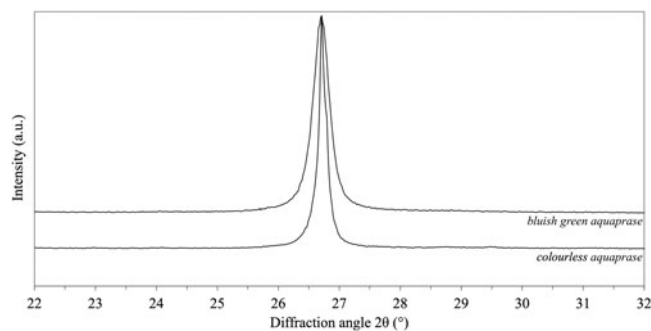


Figure 6. Comparison between the quartz peak (101) of the bluish green fraction (top) and of the colourless fraction (bottom) of the aquaprase sample AQ_02.

peak) (Fig. 7). Quartz I has intermediate unit cell parameters with the largest crystal size and represents <10 wt.% of the bluish green aquaprase samples. In the colourless aquaprase material, the weight fractions of quartz II and quartz III decrease, whereas that of quartz I reaches 42 wt.% (Table 2), in agreement with the sharper aspect of the main quartz peak observed by laboratory powder XRD analysis (Fig. 6). Moganite, found in both colourless and bluish green aquaprase material, ranges from 22 wt.% to 30 wt.%. The synchrotron radiation results agree with observations from optical microscopy, confirming the presence of more than one variety of quartz distinguishable by grain size and morphology, and characteristic of the coloured and colourless areas of the aquaprase (Fig. 2).

High-resolution synchrotron XRD analysis on the chrysoprase samples confirmed the laboratory XRD results, revealing that the CR_01 sample is composed of quartz and moganite.

High-resolution synchrotron XRD results on agate sample AG_02 showed the highest degree of crystallinity compared to the other chalcedony varieties investigated. The XRD pattern on the same AG_02 was fitted using two quartz phases, having similar cell parameter values: one with higher average crystal size and the other with lower size. The Rietveld full-profile fit, using only one quartz variety, was unable to reach a high-quality fitting.

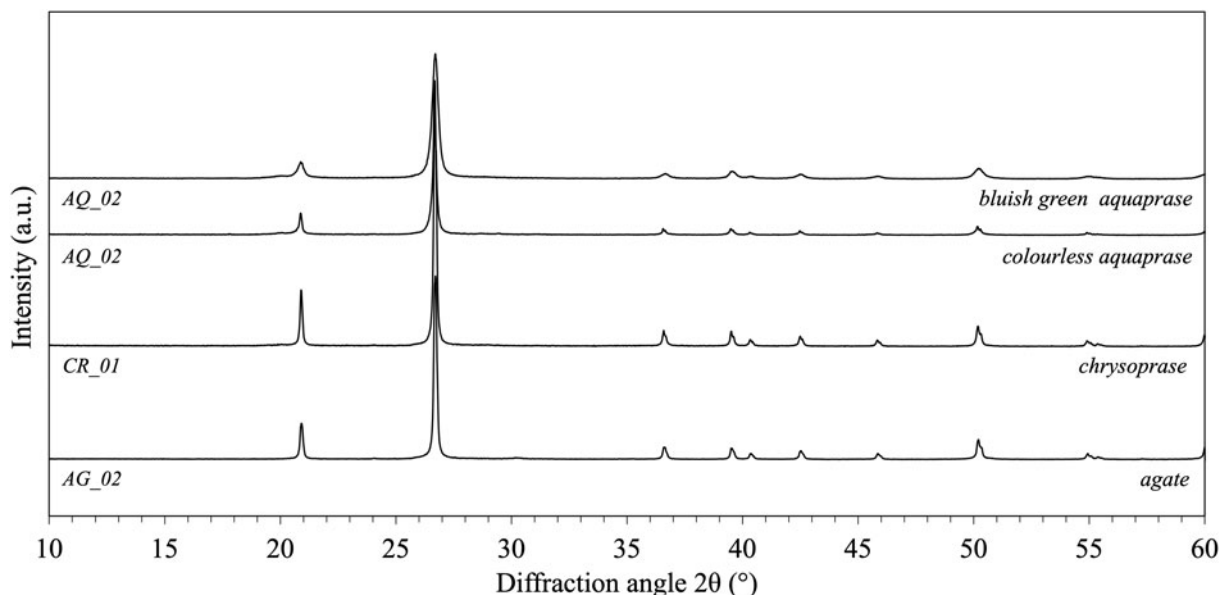


Figure 5. X-ray diffraction of powdered chalcedony samples. From top to bottom: aquaprase (bluish green and colourless fractions), chrysoprase and agate.

Table 2. Results obtained from Rietveld refinement of the diffraction patterns of aquaprase, chrysoprase and agate samples, using MAUD software.

Sample	Crystal phases					Fitting parameters*			
	quartz I	quartz II	quartz III	moganite	minor phases	Rexp (%)	Rwp (%)	Rb (%)	GOF
AQ_02 aquaprase (bluish green areas)									
Phase content [wt.%]	8.7(5)	11.5(9)	56.7(5)	22.1(6)	1.0(1)	6.25	11.49	9.02	1.84
Cell parameters [Å, °]	$a = 4.9145(4)$ $c = 5.4046(7)$	$a = 4.9688(2)$ $c = 5.3544(4)$	$a = 4.8168(3)$ $c = 5.5881(2)$	$a = 8.7046(2)$ $b = 4.9171(1)$ $c = 10.6332(1)$ $\beta = 90.6681(5)$					
Average crystal size [Å]	1800(49)	1000(240)	865(121)	358(41)					
Microstrain**	0.0032(9)	0.0043(9)	0.0063(9)	0.0128(1)					
AQ_02 aquaprase (colourless areas)									
Phase content [wt.%]	42.3(1)	19.8(5)	12.7(4)	23.4(1)	1.8(3)	7.18	14.48	11.08	2.01
Cell parameters [Å, °]	$a = 4.9137(2)$ $c = 5.4063(3)$	$a = 4.9537(1)$ $c = 5.3462(3)$	$a = 4.8385(7)$ $c = 5.5922(6)$	$a = 8.7150(7)$ $b = 4.8717(4)$ $c = 10.6767(1)$ $\beta = 90.7123(9)$					
Average crystal size [Å]	3862(250)	1315(169)	832(5)	235 (4)					
Microstrain	0.00091(5)	0.00350(9)	0.00459(4)	0.0001(1)					
AQ_03 aquaprase (bluish green areas)									
Phase content [wt.%]	9.3(2)	12.4(7)	46.3(2)	30.7(5)	1.3(8)	6.41	9.10	6.90	1.42
Cell parameters [Å, °]	$a = 4.9163(6)$ $c = 5.4061(9)$	$a = 4.9807(2)$ $c = 5.3431(5)$	$a = 4.7051(6)$ $c = 5.9182(2)$	$a = 8.5840(1)$ $b = 4.8773(5)$ $c = 10.8778(4)$ $\beta = 90.1027(3)$					
Average crystal size [Å]	2600(122)	1500(194)	769(8)	135(4)					
Microstrain	0.00066(2)	0.00514(9)	0.00326(3)	0.00615(8)					
CR_01 chrysoprase									
Phase content [wt.%]	88.15(4)	–	–	8.99(9)	2.85(8)	5.64	10.45	8.27	1.85
Cell parameters [Å, °]	$a = 4.9146(2)$ $c = 5.4062(2)$	–	–	$a = 8.6709(9)$ $b = 4.8717(5)$ $c = 10.7570(1)$ $\beta = 90.6868(9)$					
Average crystal size [Å]	2027(4)	–	–	304(8)					
Microstrain	0.0006(1)	–	–	0.0009(2)					
AG_02 agate									
Phase content [wt.%]	56.51(3)	43.49(7)	–	–	–	5.07	12.06	9.16	2.38
Cell parameters [Å, °]	$a = 4.9144(2)$ $c = 5.4059(2)$	$a = 4.9159(9)$ $c = 5.4072(2)$	–	–	–				
Average crystal size [Å]	10150(2)	940(7)	–	–	–				
Microstrain	0.00018(3)	0.00086(2)	–	–	–				

* Rexp: R-expected, Rwp: R-weighted pattern, Rb: R-profile, GOF: Goodness of Fit; as defined in MAUD.

**Microstrain is a dimensionless parameter, as defined in MAUD, due to the magnitude of dislocations, vacancies, defects and chemical impurities affecting the crystal structure. The peak broadening due to microstrain varies as: $\beta_{\text{re}} = 4\epsilon \tan\theta_i$ (where β_{re} is the integral breadth for the Gaussian component of the sample broadening and ϵ is the rms microstrain)

'-' = not determined

These results agree with the optical observations that revealed the presence of two varieties of quartz with different crystallinity (Fig. 4b).

Micro-Raman spectroscopy

Raman spectra revealed the presence of the two silica polymorphs, α -quartz and moganite, in the samples of the three gem varieties of chalcedony (Fig. 8). Due to the similar crystal structure of these two phases, their Raman spectra show several signal overlaps. They are usually distinguished by the position of the signal related to the main Si–O–Si bending vibration, at 465 cm^{-1} and 501 cm^{-1} for α -quartz and moganite, respectively (Kingma and Hemley, 1994; Heaney *et al.*, 2007). The full Raman spectrum file (from 150 to 950 cm^{-1}) of the chalcedony sample has been deposited and is available as Supplementary material (see below).

The normalised spectra (to the quartz most intensive peak) show a higher relative intensity of the main moganite peak in the aquaprase variety than in the chrysoprase and agate varieties. At first instance, this difference could be interpreted as a sign of

a higher concentration of moganite in the new chalcedony variety, although changes in the peak intensity at 501 cm^{-1} may also originate from the different content of Si(OH) groups and, therefore, quantitative phase analysis of moganite by vibrational spectroscopy should be carried out carefully (Schmidt *et al.*, 2013a).

In the Raman spectrum of chrysoprase, the peak observed at 675 cm^{-1} is ascribable to the willemseite phase which, as mentioned above, is a common inclusion and the cause of the intense apple-green colouration of this chalcedony variety (Majumdar *et al.*, 2014). According to Eggleton *et al.* (2011), despite the importance of willemseite as a colouring agent in chrysoprase, it usually occurs as small and scattered inclusions with an average concentration of $\sim 5\text{ wt.}\%$. This low value may explain the weak relative intensity of its signal in the Raman spectrum.

Electron microprobe analysis

Back-scattered electron images of the aquaprase variety confirm the microstructure observed by optical microscopy on the coloured and colourless areas (Fig. 9a compared to Fig. 2a).

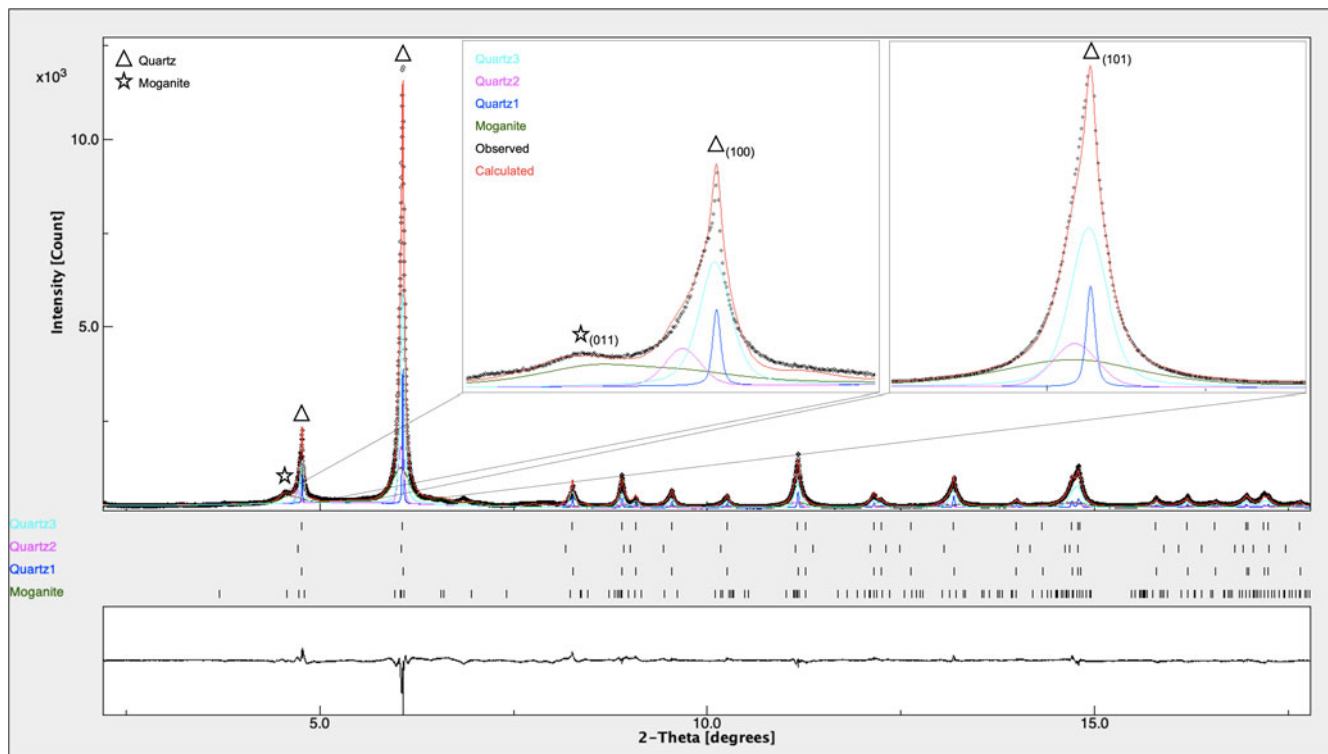


Figure 7. MAUD software interface: main quartz diffraction peaks (101) and (100) and moganite peak (011) in the aquaprase pattern. Only by using three varieties of quartz (with different degree of crystallinity and unit cell parameters) and moganite, it is possible to obtain the best fit of the aquaprase pattern.

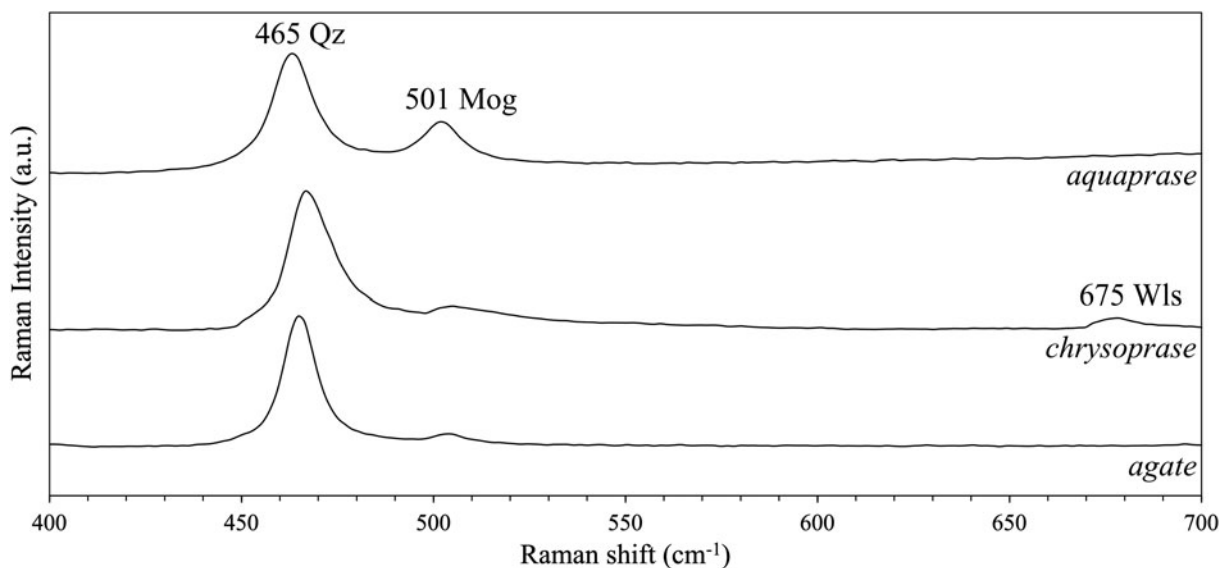


Figure 8. Normalised Raman spectra detail of the AQ_01 aquaprase sample, CR_01 chrysoprase sample and AG_01 agate ($400\text{--}700\text{ cm}^{-1}$), with the main signals of quartz and moganite.

Compositional point analyses on different samples of aquaprase, chrysoprase and agate gave a dominant SiO_2 composition with low contents of other elements, except for chrysoprase, which contained variable NiO (up to 5 wt.%) in the brighter zones shown in Fig. 9b. The calculated stoichiometric formulas, based on 2 oxygen atoms per formula unit (apfu), show lower silicon contents and the presence of other elements such as Al, Na, K and Mg in the coloured areas with the microcrystalline aspect

of aquaprase, and no compositional variations corresponding to the typical banded zones of agates (Fig. 9c), which show the lowest content both of minor and trace elements. Compositions of the different samples are reported in Table 3.

Compositional maps of Ni and Mg in CR_01 are shown in Fig. 10, which support the hypothesis of Eggleton *et al.* (2011) on the content of Ni and Mg in chrysoprase, potentially ascribable to the presence of willemseite, $(\text{Ni,Mg})_3\text{Si}_4\text{O}_{10}(\text{OH})_2$, occurring

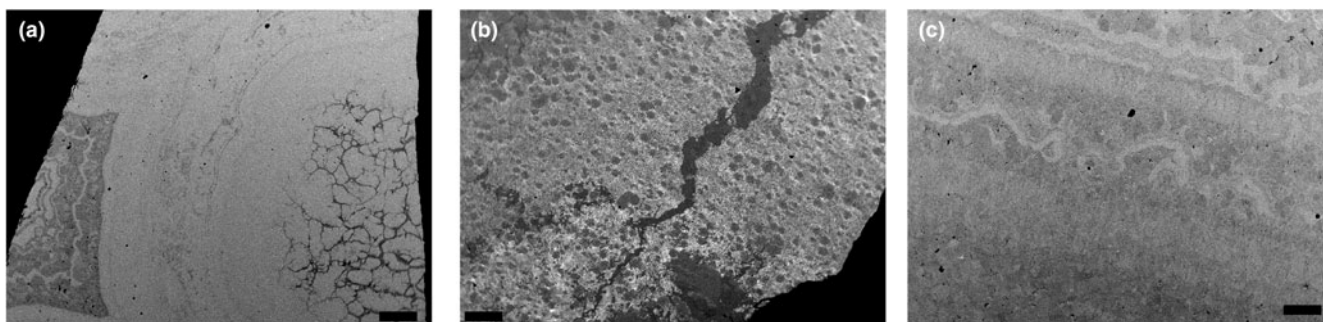


Figure 9. BSE images of (a) AQ_01, (b) CR_01 and (c) AG_01. Scale bar corresponds to 200 µm.

Table 3. Selected compositional formulas, based on the electron microprobe analyses, of different samples (calculated on 2 oxygen apfu).

Cation	AQ_01 bluish green	AQ_01 colourless	CR_01	AG_01
Si ⁴⁺	0.949	0.999	0.976	0.999
Al ³⁺	0.024	0.001	0.001	–
Na ⁺	0.038	0.001	–	–
K ⁺	0.021	–	–	–
Mg ²⁺	0.033	–	0.002	–
Ni ²⁺	–	–	0.045	–

‘–’ = not detected

as 30–100 nm-wide zones, largely aligned on polycrystalline quartz grain boundaries.

Laser ablation inductively coupled plasma mass spectrometry

The trace-element composition investigated by LA-ICP-MS of aquaprase (at bluish green and colourless areas), apple green chrysoprase and light-blue banded agate are reported in Table 4 (trace-element values detected in concentrations ≥ 1 ppm).

The aquaprase variety is characterised by significant concentrations of Mg and Al, particularly in the bluish green areas (with a maximum of 12,300 ppm and 9460 ppm, respectively). High concentrations of Ca and significant values of Na and K were also revealed. These two latter elements have relatively constant values in the different coloured areas of the samples (with a maximum of 4450 ppm, 1820 ppm and 2750 ppm, respectively). Regarding the chromophore elements, Cr has the highest concentrations (with a maximum of 2700 ppm), followed by Fe (1750 ppm) and Ni (536 ppm), which are significantly higher in the bluish green areas of the samples.

High concentrations of Ti (with a maximum of 2660 ppm) were measured in the colourless areas of the samples. Finally, chemical analysis also revealed the presence of U in concentrations as low as a few parts per million (with an average of 1 ppm) and with slightly higher values in the colourless areas of the samples, where it reaches a maximum of 5 ppm.

Analyses performed on the visible brown and opaque inclusions in the aquaprase samples revealed high concentrations of Ca, Ti and Fe (with maximum values of 17,100 ppm, 7700 ppm and 2890 ppm, respectively).

A positive correlation was observed among the trends of the main elements (Fig. 11). It is particularly evident between Al and Mg and between Al and Cr. This positive linear correlation is proven by the R^2 value of the linear function describing the trends, ($R^2 = 0.983$ and $R^2 = 0.907$ respectively) (Fig. 11a). Regarding the relationship among the trends of the chromophores, the positive correlation is evident for Cr and Ni ($R^2 = 0.923$) while not between Cr and Fe ($R^2 = 0.612$) (Fig. 11b). The chemical characterisation at the nanoscale of the aquaprase samples, performed by TEM confirmed the results obtained by LA-ICP-MS investigation. The main trace elements, Al, Mg, Na, K, are revealed simultaneously and almost ubiquitously. As for chromium, the main chromophore element, EDS analysis revealed its presence concurrently with the other mentioned trace elements and Fe and Ni, even if it is found locally in isolated points of analysis, rather than diffusely.

The chrysoprase variety shows prominent Ni concentrations (average 8450 ppm, with a maximum of 17,500 ppm) and significant concentrations of Mg, Ca and Na were also revealed.

The agate variety shows an overall pure and homogeneous chemical composition, with low concentrations of Ca (109–405 ppm), Na (25–306 ppm) and the only chromophore element Fe (8–54 ppm).

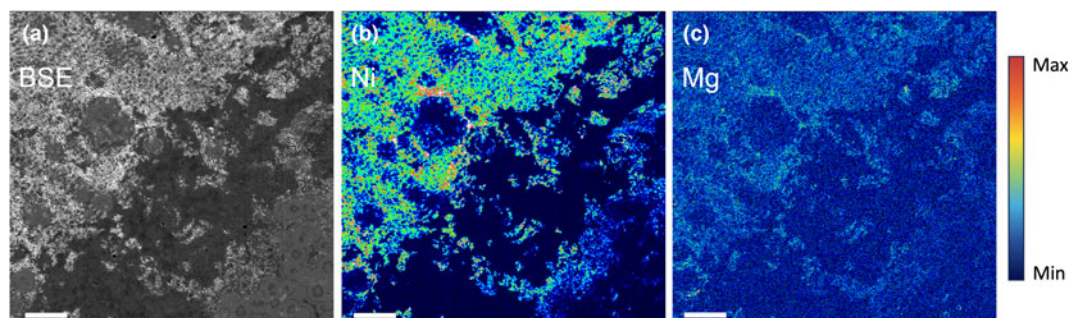
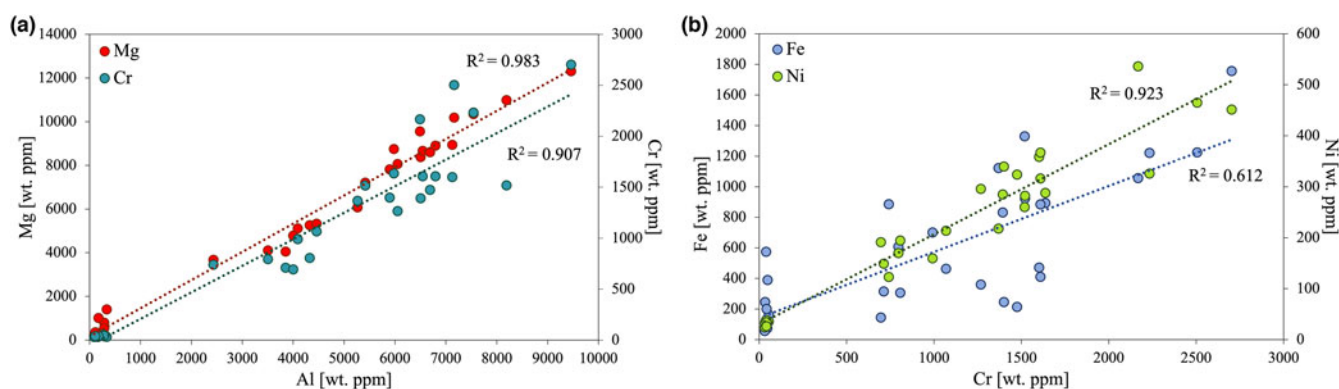


Figure 10. Element distribution maps of CR_01 chrysoprase sample: (a) BSE image; (b) Ni content; and (c) Mg content. Scale bar corresponds to 100 µm.

Table 4. Average trace-element composition (ppm) as detected by LA-ICP-MS of aquaprase (3 samples), chrysoprase (2 samples) and agate (2 samples) investigated.

	Aquaprase				Chrysoprase		Agate	
	Bluish green areas		Colourless areas		Average	Range n = 10	Average	Range n = 15
	Average	Range n = 14	Average	Range n = 10				
Li	2	1–7	1	bdl–2	bdl	bdl–bdl	bdl	bdl–1
B	6	2–14	7	4–14	4	3–6	12	5–20
Na	193	28–1091	851	147–1820	96	64–157	79	25–306
Mg	6591	1689–12314	607	227–1408	170	63–157	3	bdl–13
Al	4902	938–9463	213	46–336	bdl	bdl–2	5	bdl–16
K	223	89–516	2479	233–2750	63	26–204	13	3–49
Ca	1059	411–4452	2017	788–3615	134	80–205	238	109–405
Sc	18	9–33	6	3–8	1	1–1	1	1–1
Ti	129	4–1212	912	128–2661	bdl	bdl–bdl	5	1–28
V	4	2–6	4	bdl–11	bdl	bdl–bdl	bdl	bdl–1
Cr	1253	502–2703	10	1–24	23	2–56	1	1–2
Mn	2	1–11	2	bdl–6	1	1–1	1	bdl–4
Fe	693	145–1757	192	37–555	15	10–27	20	8–54
Co	5	1–19	1	bdl–1	1	bdl–1	bdl	bdl–bdl
Ni	280	80–536	13	4–19	8450	951–17544	3	bdl–25
Cu	6	1–37	27	12–67	2	bdl–4	8	bdl–33
Zn	24	34790	74	25–251	23	3–46	1	bdl–3
Sr	2	1–4	2	1–4	bdl	bdl–bdl	bdl	bdl–bdl
Zr	11	2–28	1	bdl–1	bdl	bdl–bdl	43	21–60
Ba	7	2–11	1	1–3	bdl	bdl–bdl	bdl	bdl–bdl
U	1	bdl–3	1	bdl–5	bdl	0	bdl	bdl–1

bdl: below detection limit

**Figure 11.** Correlation among main elements revealed in the aquaprase variety (> 1 wt. ppm): (a) Al vs Mg and Al vs Cr; (b) Cr vs Fe and Cr vs Ni.

Discussion

In this research, we conducted a comprehensive characterisation of three commonly utilised chalcedony varieties in gemmology: aquaprase, agate and chrysoprase. Specifically, we focused on a detailed examination of the mineralogical, chemical, and microstructural attributes of aquaprase, which represents a novel chalcedony variety distinguished by its colour inhomogeneity. In aquaprase, the complex mineralogical assemblage characterised by three varieties of stable (α -quartz) and one metastable (moganite) silica phases and their morphologies (i.e. fibrous, granular, crypto-, micro- and macrocrystalline) is the result of formation processes and the following recrystallisation phenomena of silica, which form metastable phases, with high solubility and low structural order, turned into macrocrystalline and stable phases with low solubility and high structural order (Gliozzo, 2019; Moxon and Palyanova, 2020). Compositional variations in aquaprase

exhibit correlations with the structural ones and affect the colouration of this variety of chalcedony.

The high concentration of Al found ubiquitously in aquaprase samples could be related to the substitution of Si by Al in the crystal structure of quartz. Aluminium is the most frequent trace element in quartz, occurring at levels of up to a few thousand ppm, due to its common presence in the Earth's crust and the similar ionic radii of Si^{4+} and Al^{3+} (Götze, 2009). Na^+ and K^+ can be found as extra-framework populations in the structure of quartz, offsetting the charge of trivalent substituent ions (such as Al^{3+}), but they are also commonly hosted by characteristic mineral micro-inclusions. Given the high concentration values of Al and Mg and their strong positive correlation, it is probable that their contribution is also caused by the presence of mineral inclusions (e.g. minor phases observed throughout the X-ray diffraction analysis, such as palygorskite). The same happens with the high calcium contents that suggest the presence of inclusions.

Chemical analysis of the trace elements showed that the cause of the bluish green colouration of aquaprase is the chromophore element Cr, which is consistently present in significant amounts in the coloured areas of all samples (reaching a maximum of 2703 ppm). Chromium could be found in the form of ions Cr^{3+} in a proper extra-framework site of the crystal structure of quartz, but due to the Cr ion size and its high concentration in the samples, it seems more reasonable that this element is characteristic of nano inclusions (Hyrsly, 1999). In particular, the strong positive correlation between Cr and Ni suggests that these inclusions could be Ni–Cr bearing minerals (e.g. spinel).

Regarding the Fe concentration, its presence is related to the numerous dark, opaque inclusions, probably in the form of iron oxides.

Titanium is one of the elements for which the substitution $\text{Ti}^{4+} \rightleftharpoons \text{Si}^{4+}$ has been demonstrated (Götze, 2009). The ionic radius of Ti^{4+} is relatively large, which leads to its preferential incorporation into the marginal parts of crystals (Götze and Plötze, 1997). Nevertheless, the significant concentration of this element could be due to the presence of inclusions, such as Ti-oxide (e.g. rutile) or Fe–Ti-oxide (e.g. ilmenite).

Uranium is found frequently in chalcedony and opal as the uranyl ion bonded to H_2O molecules, as noted by Modreski (1987) and Götze *et al.* (2015). Its presence is associated primarily with the transportation of chemical elements (such as Al, Ca, Fe, K, Na and B) during late volcanic and post-volcanic alteration processes, consequently accumulating during the process of chalcedony formation. The presence of uranium causes a green fluorescence effect visible at concentrations of U even below 1 ppm (I. Adamo, pers. comm.).

The chrysoprase variety exhibits a more homogeneous chemical and mineralogical composition and microstructural setting; the intense apple-green colouration is due to the presence of nickel phyllosilicate inclusions. The high concentration of Ni revealed is consistent with the occurrence of Ni-bearing layered silicate minerals (Eggleton *et al.*, 2011), confirming the presence of willemsite, highlighted by micro-Raman spectroscopy, and dispersed irregularly in the silica aggregate.

Finally, the banded appearance, typical of Turkish agate, is not related to trace/minor chromophore elements (iron in particular), but rather to the different grain size and morphology of quartz crystals, as also suggested by Lorenzi *et al.* (2022).

In conclusion, this study demonstrates that the distinct colouration observed in the three different varieties of chalcedony cannot be attributed exclusively to a single cause, such as the presence of chromophores. Instead, it is probably the result of a combination of several features, such as chromophores, inclusion or microstructure. Only through a multidisciplinary approach can these factors be brought to light and thoroughly understood. In particular, by integrating mineralogical, chemical, microstructural analyses, a comprehensive understanding of the intricate processes and elements influencing the colours exhibited by aquaprase, agate and chrysoprase is highlighted. This approach is essential to unravel the complexities behind the visual appeal of these gemstones and to advance our knowledge in the field of gemmology.

Acknowledgements. We acknowledge the European Synchrotron Radiation Facility (ESRF) for the provision of synchrotron radiation facilities, and we thank the staff for assistance and support in using beamline ID22. The authors also thank prof. Rosangela Bocchio for her suggestions. Funding for this research was provided by: Italian Ministry of Education (MIUR) (PRIN2017 - Mineral reactivity, a key to understand large-scale processes: award No.

2017 L83S77) and “Dipartimenti di Eccellenza 2023–2027 – “Le Georisorse per la transizione ecologica e lo sviluppo territoriale”.

Supplementary material. The supplementary material for this article can be found at <https://doi.org/10.1180/mgm.2023.92>.

Competing interests. The authors declare none.

References

- Adams S.F. (1920) A microscopic study of vein quartz. *Economic Geology*, **15**, 623–664.
- Adams A.E., MacKenzie W.S. and Guilford C. (1984) *Atlas of Sedimentary Rocks Under the Microscope*. Routledge, New York [pp. 6, 85].
- Bambauer H.U., Brunner G.O. and Laves F. (1961) Beobachtungen über Lamellenbau an Bergkristallen. *Zeitschrift für Kristallographie*, **116**, 173–181.
- Cady S.L., Wenk H.R. and Sintubin M. (1998) Microfibrous quartz varieties: characterization by quantitative X-ray texture analysis and transmission electron microscopy. *Contributions to Mineralogy and Petrology*, **130**, 320–335.
- Caucia F., Marinoni L., Ghisoli C. and Leone A. (2016) Gemological, physical and chemical properties of prase opals from Hanety Hill (Tanzania). *Periodico di Mineralogia*, **85**, 41–50.
- Čermáková Z., Hradil D., Bezdička P. and Hradilová J. (2017) New data on “kerolite–pimelite” series and the colouring agent of Szklary chrysoprase, Poland. *Physics and Chemistry of Minerals*, **44**, 193–202.
- Chiari G., Giustetto R. and Ricchiardi G. (2003) Crystal structure refinements of palygorskite and Maya Blue from molecular modelling and powder synchrotron diffraction. *European Journal of Mineralogy*, **15**, 21–33.
- Conte A., Della Ventura G., Rondeau B., Romani M., Cestelli Guidi M., La C., Napoleoni C. and Lucci F. (2022) Hydrothermal genesis and growth of the banded agates from the Allumiere-Tolfa volcanic district (Latium, Italy). *Physics and Chemistry of Minerals*, **49**, 39.
- De Waal S.A. (1970) Nickel minerals from Barberton, South Africa: III. Willemsite, a nickel-rich talc. *American Mineralogist*, **55**, 31–42.
- Dong G., Morrison G. and Jaireth S. (1995) Quartz textures in epithermal veins, Queensland; classification, origin and implication. *Economic Geology*, **90**, 1841–1856.
- Eggleton R.A., Fitz Gerald J. and Foster L. (2011) Chrysoprase from Gumigil, Queensland. *Australian Journal of Earth Sciences*, **58**, 767–776.
- Flörke O.W., Jones J.B. and Schmincke H.U. (1976) A new microcrystalline silica from Gran Canaria. *Zeitschrift für Kristallographie – Crystalline Materials*, **143**, 156–165.
- Flörke O.W., Köhler-Herbertz B., Langer K. and Tönges I. (1982) Water in microcrystalline quartz of volcanic origin: agates. *Contributions to Mineralogy and Petrology*, **80**, 324–333.
- Gliozzo E. (2019) Variations on the silica theme: Classification and provenance from Pliny to current supplies. *The Contribution of Mineralogy to Cultural Heritage*, **20**, 13–85.
- Gliozzo E., Cairncross B. and Vennemann T. (2019) A geochemical and micro-textural comparison of basalt-hosted chalcedony from the Jurassic Drakensberg and Neoproterozoic Ventersdorp Supergroup (Vaal River alluvial gravels), South Africa. *International Journal of Earth Sciences*, **108**, 1857–1877.
- Götze J. (2009) Chemistry, textures and physical properties of quartz-geological interpretation and technical application. *Mineralogical Magazine*, **73**, 645–671.
- Götze J. and Plötze M. (1997) Investigation of trace-element distribution in detrital quartz by Electron Paramagnetic Resonance (EPR). *European Journal of Mineralogy*, **9**, 529–538.
- Götze J., Gaft M. and Möckel R. (2015) Uranium and uranyl luminescence in agate/chalcedony. *Mineralogical Magazine*, **79**, 985–995.
- Graetsch H. (1994) Structural characteristics of opaline and microcrystalline silica minerals. Pp. 209–232 in: *Silica: Physical Behavior, Geochemistry, and Materials Applications* (Peter J. Heaney, Charles T. Prewitt, and Gerald V. Gibbs, editors). Reviews in Mineralogy, **29**. Mineralogical Society of America, Washington, DC.
- Gražulis S., Daškevič A., Merkys A., Chateigner D., Lutterotti L., Quirós M., Serebryanaya N.R., Moeck P., Downs R.T. and Le Bail A. (2012)

- Crystallography Open Database (COD): an open-access collection of crystal structures and platform for world-wide collaboration. *Nucleic Acids Research*, **40**(D1), D420–D427.
- Gruner J.W. (1934) The crystal structures of talc and pyrophyllite. *Zeitschrift für Kristallographie – Crystalline Materials*, **88**, 412–419.
- Hatipoğlu M., Ören U. and Kibici Y. (2011) Micro-Raman spectroscopy of gem-quality chrysoprase from the Biga-Çanakkale region of Turkey. *Journal of African Earth Sciences*, **61**, 273–285.
- Heaney P.J. (1993) A proposed mechanism for the growth of chalcedony. *Contributions to Mineralogy and Petrology*, **115**, 66–74.
- Heaney P.J. and Post J.E. (1992) The widespread distribution of a novel silica polymorph in microcrystalline quartz varieties. *Science*, **255**(5043), 441–443.
- Heaney P.J. and Post J.E. (2001) Evidence for an *I2/a* to *Imab* phase transition in the silica polymorph moganite at ~570 K. *American Mineralogist*, **86**, 1358–1366.
- Heaney P.J., McKeown D.A. and Post J.E. (2007) Anomalous behavior at the *I2/a* to *Imab* phase transition in SiO₂-moganite: an analysis using hard-mode Raman spectroscopy. *American Mineralogist*, **92**, 631–639.
- Hyrsl J. (1999) Chrome chalcedony – a review. *The Journal of Gemmology*, **26**, 364–370.
- Jiang Y. and Guo Y. (2021) Genesis and influencing factors of the colour of chrysoprase. *Scientific Reports*, **11**, 9939.
- Jiang Y., Guo Y., Zhou Y., Li X. and Liu S. (2021) The effects of Munsell neutral grey backgrounds on the colour of chrysoprase and the application of AP clustering to chrysoprase colour grading. *Minerals*, **11**, 1092.
- Jóźwiak-Niedźwiedzka D., Gibas K. and Glinicki M.A. (2017) Petrographic identification of reactive minerals in domestic aggregates and their classification according to RILEM and ASTM recommendations. *Roads and Bridges-Drogi i Mosty*, **16**, 223–239.
- Kingma K.J. and Hemley R.J. (1994) Raman spectroscopic study of microcrystalline silica. *American Mineralogist*, **79**, 269–273.
- Lignie A., Granier D., Armand P., Haines J. and Papet P. (2012) Modulation of quartz-like GeO₂ structure by Si substitution: An X-ray diffraction study of Ge_{1-x}Si_xO₂ (0 ≤ x < 0.2) flux-grown single crystals. *Journal of Applied Crystallography*, **45**, 272–278.
- Lorenzi R., Zullino A., Gagliardi V., Prosperi L., Paleari A. and Adamo I. (2022) Atomic and microstructural origin of banded colours in purple-blue variety of agate from Yozgat Province, Turkey. *Physics and Chemistry of Minerals*, **49**, 33.
- Lutterotti L., Bortolotti M., Ischia G., Lonardelli I. and Wenk H.R. (2007) Rietveld texture analysis from diffraction images. *Zeitschrift für Kristallographie Supplement*, **26**, 125–130.
- Majumdar A.S., King H.E., John T., Kusebauch C. and Putnis A. (2014) Pseudomorphic replacement of diopside during interaction with (Ni, Mg) Cl₂ aqueous solutions: Implications for the Ni-enrichment mechanism in talc-and serpentine-type phases. *Chemical Geology*, **380**, 27–40.
- Michel-Lévy A. and Munier-Chalmas E. (1892) Mémoire sur diverses formes affectées par le réseau élémentaire du quartz. *Bulletin de Minéralogie*, **15**, 159–190.
- Miehe G. (1986) Moganit: Strukturvorschlag für ein neues mikrokristallines SiO₂-Mineral. *Fortschritte der Mineralogie*, **64**, 117.
- Miehe G. and Graetsch H. (1992) Crystal structure of moganite: a new structure type for silica. *European Journal of Mineralogy*, **4**, 693–706.
- Miehe G., Graetsch H. and Flörke O.W. (1984) Crystal structure and growth fabric of length-fast chalcedony. *Physics and Chemistry of Minerals*, **10**, 197–199.
- Modreski P.J. (1987) Ultraviolet fluorescence of minerals, examples from New Mexico. *New Mexico Geology*, **9**, 25–30.
- Moxon T. and Palyanova G. (2020) Agate genesis: A continuing enigma. *Minerals*, **10**, 953.
- Renfro N. (2015) A new natural-color bluish green chalcedony. *Gems & Gemology*, **51**, 452–454.
- Ríos S., Salje E.K.H. and Redfern S.A.T. (2001) Nanoquartz vs. macroquartz: a study of the α ↔ β phase transition. *The European Physical Journal B-Condensed Matter and Complex Systems*, **20**, 75–83.
- Sachanbiński M., Janeczek J., Platonov A. and Rietmeijer F.J. (2002) The origin of colour of chrysoprase from Szklary (Poland) and Sarykul Boldy (Kazakhstan). *Neues Jahrbuch für Mineralogie-Abhandlungen*, **177**, 61–76.
- Saville A.I., Creuziger A., Mitchell E.B., Vogel S.C., Benzing J.T., Klemm-Toole J., Clarke K.D. and Clarke A.J. (2021) MAUD Rietveld refinement software for neutron diffraction texture studies of single-and dual-phase materials. *Integrating Materials and Manufacturing Innovation*, **10**, 461–487.
- Schmidt P., Bellot-Gurlet L., Léa V. and Sciau P. (2013a) Moganite detection in silica rocks using Raman and infrared spectroscopy. *European Journal of Mineralogy*, **25**, 797–805.
- Schmidt P., Slodczyk A., Léa V., Davidson A., Puaud S. and Sciau P. (2013b). A comparative study of the thermal behaviour of length-fast chalcedony, length-slow chalcedony (quartzine) and moganite. *Physics and Chemistry of Minerals*, **40**, 331–340.
- Steinfink H. (1962) Crystal structure of a trioctahedral mica: phlogopite. *American Mineralogist: Journal of Earth and Planetary Materials*, **47**, 886–896.
- Warr L.N. (2021) IMA-CNMNC approved mineral symbols. *Mineralogical Magazine*, **85**, 291–320.
- White J.F. and Corwin J.F. (1961) Synthesis and origin of chalcedony. *American Mineralogist: Journal of Earth and Planetary Materials*, **46**, 112–119.